Materials and Design 182 (2019) 107966

Contents lists available at ScienceDirect

Materials and Design

journal homepage: www.elsevier.com/locate/matdes

Design and impact response of 3D-printable tensegrity-inspired structures

Kirsti Pajunen[a,*], Paul Johanns[a], Raj Kumar Pal[b], Julian J. Rimoli[b], Chiara Daraio[a]

[a]Department of Mechanical and Civil Engineering, California Institute of Technology, Pasadena, CA, USA
[b]School of Aerospace Engineering, Georgia Institute of Technology, Atlanta, GA, USA

HIGHLIGHTS

- We present the design of a 3D-printable structure with comparable response characteristics as a pin-jointed tensegrity structure.
- Drop weight simulations and experiments show unique and desirable impact characteristics.
- Theoretical studies on tensegrity structures with elastically buckling struts are corroborated experimentally for the first time.
- These studies pave the way for new research in the area of manufacturable tensegrity-inspired metamaterials.

GRAPHICAL ABSTRACT

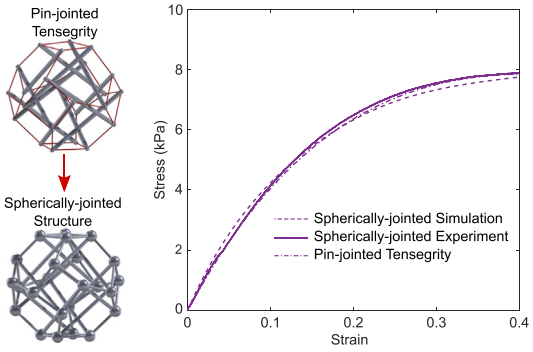

ARTICLE INFO

Article history:
Received 13 March 2019
Received in revised form 25 May 2019
Accepted 23 June 2019
Available online 2 July 2019

Keywords:
Tensegrity
Metamaterials
Dynamic impact
3D-printing
Buckling
Architected unit cells

ABSTRACT

Recent studies demonstrate the potential of tensegrity structures as unique building blocks for architected lattices (metamaterials). Key tensegrity characteristics, such as elastic response under severe deformation, high strength-to-weight ratio, and nonlinear behavior, make these structures appealing for dynamic applications. A new method of tessellating tensegrity unit cells with elastically buckling struts in three dimensions has opened new avenues for metamaterials with superior mechanical properties. However, traditional fabrication methods for tensegrity structures are cumbersome and do not allow accurate control of the level of member prestress. To overcome these limitations, we present a design of a 3D-printable, single material structure which has comparable strain energy capacity and compressive response as a tensegrity structure with buckling struts. The structure's geometry maintains key tensegrity characteristics, thus generating an equivalent mechanical response. Numerical simulations inform quasi-static compression experiments and dynamic drop weight impact tests. The structure's responses correspond well to the pin-jointed tensegrity, exhibiting desirable characteristics such as post-buckling stability, resilience under severe deformation, high elastic strain energy absorption, and load-limitation. This work is the first to experimentally corroborate theoretical studies of buckling tensegrity structures. We conjecture that the structure presented here has unique potential as a unit cell for manufacturable tensegrity-inspired metamaterials.

1. Introduction

Tensegrity structures have been described as islands of compression among a sea of tension [1]. They consist of two types

* Corresponding author.
E-mail address: kpajunen@caltech.edu (K. Pajunen).

https://doi.org/10.1016/j.matdes.2019.107966

of axially-loaded pin-jointed members: isolated, stiff struts in compression and a continuous arrangement of cables in tension. Tensegrity structures appear similar to truss structures but have the important difference that they must carry prestress in the members to carry external load [2]. Tensegrity structures have many appealing characteristics for engineering applications. They are lightweight, energy and mass efficient, often deployable, robust to failure, and able to withstand large deformations [3-15]. Under dynamic loading, these structures have been shown to be impact tolerant and possess unique nonlinear responses [16-23].

The traditional definition of a tensegrity structure assumes that the struts are stiff, are not free to buckle, and do not store energy. Tensegrity structures with elastically buckling struts have been recently studied using physics-based reduced-order models, and their mechanical response has been characterized under static and dynamic loads [16]. In this case, the struts undergo large deformation due to buckling, contributing to the strain energy of the structure. There are many advantageous properties associated with this. First, the load is distributed among all the members in the structure, increasing structural efficiency. Second, the strain energy capacity of the structure (the area under the stress-strain curve) is dramatically increased because the stress-strain curve plateaus due to buckling in the struts. Finally, the structure can undergo severe deformation and recover its initial configuration upon unloading due to elastic buckling in the struts [16].

Structured materials (or metamaterials) composed of periodic arrays of architected building blocks have been recently explored as alternatives to stochastic foams in energy absorption applications [24-26]. Metamaterial building blocks exploit local deformations, like buckling of members, to convey unique global properties to the bulk material. The selection of appropriate building block geometries allows tailoring the mechanical properties to achieve desired characteristics. The unique static and dynamic behavior of tensegrity structures make them appealing as metamaterial building blocks. One-dimensional chains of tensegrity unit cells have been shown to possess unique nonlinear wave propagation properties [27-30] and unconventional and tunable bandgap structures [31,32]. The formation of 3D lattices has been elusive due to inadequate symmetries of tensegrity structures. However, a new method has overcome previous limitations by tessellating a tensegrity unit cell based on a truncated octahedron in three dimensions while maintaining isolated compression loops [33]. These buckling 3D lattices possess superior static and dynamic mechanical properties. Considering these studies, tensegrity-based metamaterials have significant potential for energy absorption, wave management, and a variety of other dynamic applications [34,35].

A way to manufacture such lattices for applications and experimentally corroborate existing theoretical studies on these structures [16] has remained elusive, due to the pin-jointed and prestressed nature of tensegrity structural members. Most work has relied on manual prestress and assembly [12,19,36,37]. However, in multidimensional lattices, especially at decreasing length scales and with potentially thousands of members, this approach quickly becomes impractical. Advances in 3D-printing techniques may offer more scalable solutions. It may be possible to mimic pin-jointed behavior and control prestress using multiple materials [38], shape memory materials [39], differential thermal expansion from multiple materials [40], or induced residual stresses from varying laser intensity [41].

An ideal solution to this manufacturing issue would rely on 3D-printing with a single material and no post-processing, which could enable the production of lattices with a variety of fabrication methods. In this paper, we describe a technique to design and manufacture tensegrity-inspired structures with the comparable strain energy capacity and compressive response as a buckling tensegrity structure. We then study the quasi-static and dynamic response of a selected unit cell with elastic buckling capability.

The paper is organized as follows. In Section 2, we develop a method to obtain an equivalent 3D-printable structure using a series of geometric manipulations. We describe 3 key geometry iterations to illustrate the design process. The first is given in Section 2.1, and the second and third are given in Section 2.2. This method uses a single material for the entire structure, has no post-processing, and can be adapted to a variety of printers and materials. A truncated octahedron tensegrity is used, but the method can be applied to other types of tensegrity structures as well. In Section 3, we examine the dynamic response of a selected unit cell using drop weight experiments and ABAQUS finite element simulations. We compare the dynamic response to that of a corresponding buckling tensegrity. We speculate the structure's utility as an elementary cell in multidimensional lattices based on the characteristics we observe. Finally, in Section 4, we provide a summary of the work, future directions, and implications for applications.

2. Development of equivalent structure

2.1. Rigid joints with overlapping members

The tensegrity structure described in Ref. [16] was used as the baseline pin-jointed tensegrity for this work. The structure's geometry, which is based on a truncated regular octahedron, was derived using the form-finding method described in Ref. [42]. We chose this specific architecture because it has 6 square, orthogonal "faces", which, with certain reflections required to accommodate asymmetry of the faces, allows tessellation in three-dimensional lattices [33]. We use the geometry of the un-prestressed tensegrity, noting that the geometric configuration changes based on the level of prestress applied to the cables.

The tensegrity structure is shown in Fig. 1 (a). The structure has 12 struts and 36 cables. The struts are disconnected from each other and are only connected by cables, defining it as a class 1 tensegrity [43]. In choosing the size of the baseline tensegrity, we kept in mind the manufacturing and testing constraints of the structure that we would 3D-print using the tensegrity's geometry, as described later in this section. We chose a height of 48.3 mm from the "top face" nodes to the "bottom face" nodes. We chose the cables to have a diameter of 1.37 mm and the struts a diameter of 3.05 mm, giving a strut to cable diameter ratio (d_s/d_c) of 2.23. We ensure that the chosen strut diameter allows elastic buckling by using the Euler-Johnson relation [44]:

$$\frac{L}{\rho} \geq \sqrt{\frac{2\pi E}{\sigma_y}} \tag{1}$$

where L is the length of the strut, ρ is the strut's radius of gyration, E is the Young's modulus of the material, and σ_y is the yield strength of the material. L is 44.2 mm, E is 1.29 GPa, and σ_y is 29.1 MPa. The material we chose for the structures in this paper is described and characterized later in this section.

At this point, we note that this initial pin-jointed geometry was chosen due to manufacturing constraints and to provide elastically buckling struts, not to obtain a target mechanical response. Because of this, the member diameters are altered throughout the design process, as we explain through the designs presented in Section 2. For clarity, we refer to this initial member geometry as Geometry #1, which has a d_s/d_c of 2.23.

To find an analogous 3D-printable structure, we initially fabricated Geometry #1 with rigidly overlapped members at the nodes (Fig. 1 (b)). The samples were printed with the polyamide PA2200 material from Shapeways.com © using selective laser sintering (SLS). With this method, a high-powered laser selectively fuses small particles of polymer powder together, layer by layer. The part being constructed is surrounded by powder at all times, eliminating the need for support structure. This manufacturing method was chosen for

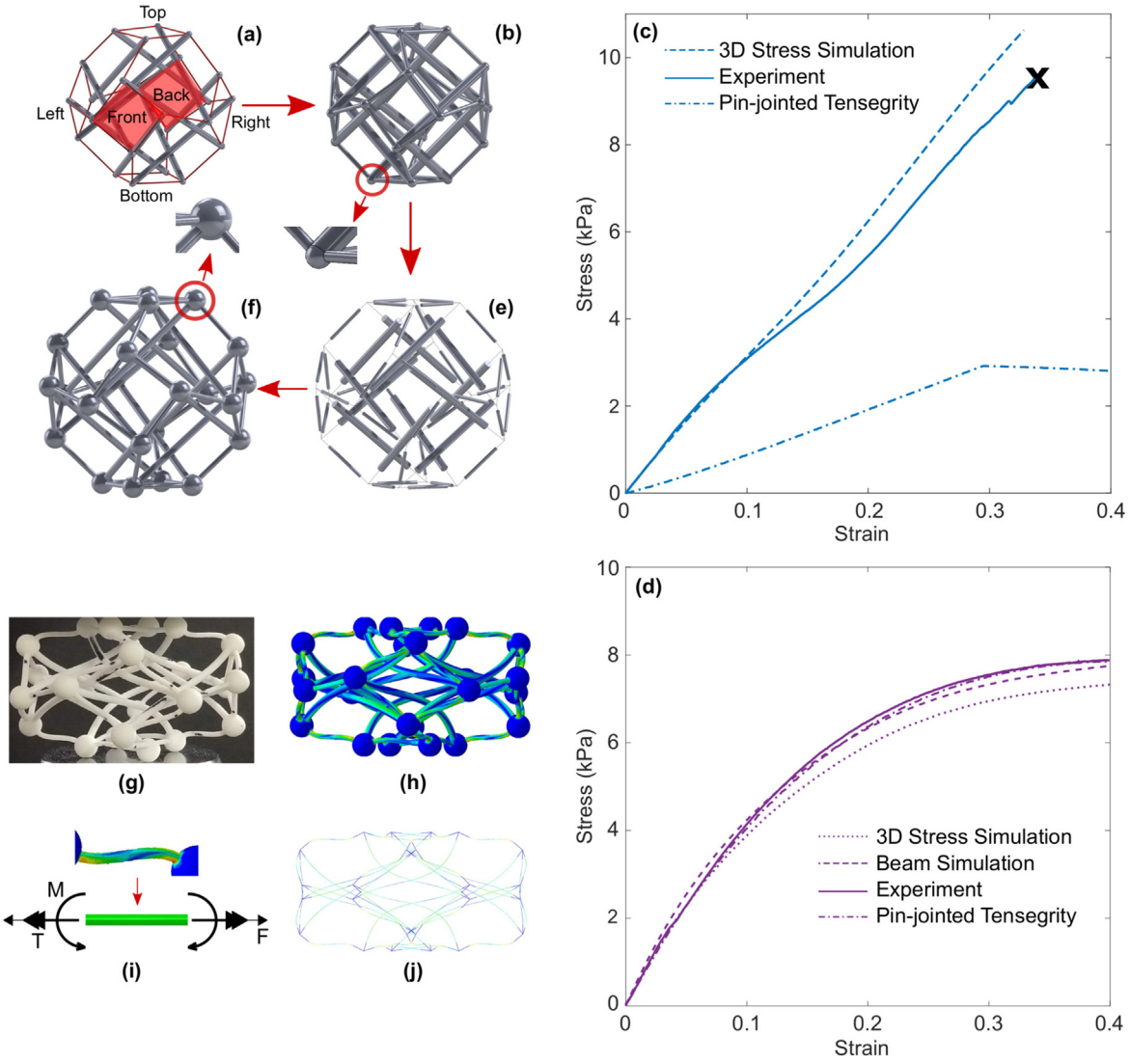

Fig. 1. (a) Pin-jointed truncated octahedron tensegrity with 6 faces. (b) 3D-printable, fixed-jointed structure with overlapping members. (c) Stress-strain curves showing the 3D stress simulation and representative experimental responses of the 3D-printable, fixed-jointed structure, as well as the response of the corresponding pin-jointed structure, all with member diameters corresponding to Geometry #1. The pin-jointed structure exhibits a clear buckling point around 0.3 strain, whereas the fixed-jointed structure does not exhibit a buckling point, but ruptures around 0.3 strain. The stiffness of the fixed-jointed structure is much higher than the pin-jointed stiffness. This fixed-jointed structure is inadequate to represent the pin-jointed response. (d) Stress-strain curves showing responses of the 3D stress simulation, beam simulation, corresponding pin-jointed tensegrity simulation, and representative experiment. The 3D stress simulation, beam simulation, and experiment have Geometry #3, and the corresponding pin-jointed structure has Geometry #2. All four show comparable behavior, indicating the spherically-jointed structure's equivalence to a corresponding pin-jointed tensegrity structure. Nodal locations and cable lengths are maintained by (e) scaling up the structure and (f) inserting spheres at the nodes. (g) Spherically-jointed structure compressed during an experiment. (h) ABAQUS rendering of compression of the spherically-jointed structure. (i) Representation of the mechanical deformation modes exerted on the members of the spherically-jointed structure. (j) ABAQUS beam element rendering of the compression of the spherically-jointed structure. (For interpretation of the references to color in this figure, the reader is referred to the web version of this article.)

several reasons. With SLS, this structure is manufacturable with relative ease, having no support structure and no post-curing processes. The lack of post-curing also produces consistent structures with the desired constitutive material properties and mechanical responses. The chosen member diameters and aspect ratios fit well within the manufacturable limits of the SLS manufacturing method for the chosen material. We note that other 3D manufacturing approaches may also be suitable for fabrication, e.g. stereolithography (SLA), material jetting (MJ), fused deposition modeling (FDM), digital light processing (DLP), and 2-photon polymerization. We have also printed this structure with SLA and 2-photon polymerization.

To characterize the mechanical response of the fixed-jointed structure, we performed quasi-static compression experiments using an Instron E3000©. The chosen structure height of about 2 in. was a practical size for the compression experiments. The samples were loaded on the top face and compression was applied using displacement control. The top and bottom faces were allowed to rotate during compression, which occurs due to asymmetry of the face nodes.

We developed a simulation using the finite element software ABAQUS/STANDARD. A 3D model of the structure was constructed using 3D stress quadratic tetrahedral elements (element type C3D10). To allow rotation of the top and bottom faces like in the experiment, two reference points, each located at the center of the top and bottom face nodes, are kinematically coupled to their respective face nodes. The top reference point moves downward only, and the bottom reference point is fixed. This coupling constrains the vertical displacement of the 4 face nodes to the displacement of the

reference node, allowing the face nodes to rotate around the vertical axis like in the experiment. Nonlinear geometry is used to capture the large deformation buckling response. The polyamide material was characterized via tensile tests using ASTM D638 test specimens with an Instron E3000©. A hyperelastic Marlow model fitted to the experimental tensile data is used to represent the polymer's behavior. A thorough discussion of the material properties and material model are discussed in the Supplementary Material Section 1, with the constitutive tensile response shown in Supplementary Figure 1.

The stress-strain results of the ABAQUS simulation, the pin-jointed model, and a representative experiment are shown in Fig. 1 (c). The effective compressive stress-strain responses of the pin-jointed structure was found using a reduced-order model described in Ref. [16] that allows the struts to buckle and captures its nonlinear quasi-static and dynamic responses. For all structures, stress is defined as the applied load divided by the projected square cross-sectional area that intersects the face nodes. Strain is defined as the vertical displacement divided by the original height of the structure from the bottom to the top face nodes. The ABAQUS simulation and experiment are in good agreement. Both curves show a slightly nonlinear behavior, due to the relative rotation of the top and bottom faces during compression. The structures rupture at 0.3 strain, before reaching buckling, because of the high local strains at the joints.

The pin-jointed response differs significantly from the fixed-jointed structure. Without prestress, the pin-jointed structure behaves as a rigid body mechanism until reaching a critical strain (in this case, 0.25), where the members begin to carry force and deform. We subtracted this onset strain from the strain values in order to obtain the force-strain curve reported in Fig. 1 (c). The pin-jointed response has a much lower stiffness than the printed structure, and distinctly buckles at around 0.3 strain. One important difference between the fixed-jointed and the pin-jointed structures is the distribution of load. The fixed-jointed structure has complex stress states that affect the stiffness and prevent the onset of buckling. On the contrary, the members of the pin-jointed structure are loaded purely axially and hence buckle more easily. To capture the buckling response exhibited by the pin-jointed structure, a different design approach for the 3D-printable structures was needed.

2.2. Spherical joints

We target the long-term application of the 3D-printable structure to be a building block for impact absorbing periodic lattices. Although our objective for this work is not to optimize the structure for energy absorption capacity, we kept this application in mind by next adjusting the member diameters of the pin-jointed counterpart structure to obtain better elastic energy capacity. The stress-strain curve of the pin-jointed structure (with Geometry #1) in Fig. 1 (c) has an initial stiffness of about 10 kPa and buckles at around 0.3 strain. We increased the cable diameter to raise the stiffness of the structure, and increased the strut diameter to raise the buckling load and reduce the buckling strain. We also added enough prestress (2%) such that the structure is load-bearing and the struts just begin to bend at the onset of loading. We chose the cables to have a diameter of 1.8 mm and the struts a diameter of 3.32 mm, giving a d_s/d_c of 1.84. We define this as Geometry #2.

The corresponding pin-jointed stress-strain curve is seen in Fig. 1 (d) as the dash-dot purple line. The initial stiffness increased to 48 kPa. The structure now has no distinct buckling point but asymptotically approaches the buckling stress. By 0.4 strain, this structure absorbs 3.1 times the strain energy than the original structure. The original structure has a mass of 5.55 g, and the new structure has a mass of 5.75 g. Considering this mass increase of only 3.6%, the normalized strain energy by mass increases by 3 times. The transition from Geometry #1 to Geometry #2 was not to obtain a target value of strain energy absorption, but to reasonably adjust the member diameters to dramatically increase the energy absorption for the purposes of forthcoming dynamic testing and applications.

To design a 3D-printable structure with a comparable stress-strain response as the pin-jointed structure, we noted that in pin-jointed tensegrity structures, the nodal locations and member lengths are key characteristics that determine the response. In the fixed-jointed structure in Fig. 1 (b), the effective lengths of all the members are shorter than in the pin-jointed counterpart due to the overlap of the members at the nodes. The cables intersect the struts at different angles, producing varying cables lengths and large stress concentrations. The effective buckling length of the struts is thus significantly shorter than in the pin-jointed counterpart. This greatly increases the buckling load of each strut. These attributes produce the structure's high stiffness and non-buckling behavior compared to the pin-jointed counterpart.

We, therefore, redesigned the 3D-printable structure by scaling up the nodal coordinates by 1.5 (Fig. 1 (e)) and inserting spheres at the nodes (Fig. 1 (f)) with a diameter of 8.72 mm. The spheres are sized such that the cable lengths are maintained from pin-jointed Geometry #2 and so that members do not intersect. By doing this, all the cables and all the struts are the same length, and each intersects normal to the sphere. With this change, the compressive response changes dramatically. The structure's stiffness is greatly reduced, as are the maximum local strains from stress concentrations.

We performed compression tests on the spherically-jointed structure. Comparing the deformation of the compressed structure (Fig. 1 (g)) with the results obtained with ABAQUS 3D simulations (Fig. 1 (h)), we notice that each member in the structure behaves like a beam: it undergoes bending, axial loading, and torsion (Fig. 1 (i)). Each has a constant cross section and connects perpendicularly to the spheres. Because of these characteristics, we developed a simpler finite element model using beam elements. Timoshenko beam elements, which allow for transverse shear deformation and large strains, are used rather than Euler-Bernoulli elements. The type of element used is B32, which is the 3-node quadratic Timoshenko beam. In the spherically-jointed configuration, each node connects four members. To model the spheres using beam elements, a single element with the length of the radius of the sphere connects the end of each member to the node. This element is given a very large stiffness (two orders of magnitude larger than member material) and a large cross section. Using this cross section the density of the material is calculated such that the mass of all four connecting elements is the same as a sphere in the spherically-jointed structure. The top and bottom reference points and coupling with the top and bottom face nodes are the same as in the 3D stress simulation. The compressed structure with the beam element simulation is shown in Fig. 1 (j).

The pin-jointed and spherically-jointed structures have different deformation modes. In the spherically-jointed geometry, both the cables and the struts simultaneously affect the stiffness and buckling load of the structure. To achieve the target strain energy capacity of the pin-jointed counterpart structure (Geometry #2), we reduce the diameter of the struts to lower the buckling load. The final 3D-printable, spherically-jointed design has a strut diameter of 2.6 mm and a cable diameter of 1.8 mm, giving a d_s/d_c of 1.44. We define this final design as Geometry #3. It should be noted that in the design process, there were several iterations of the member diameters that we do not include in the main text for clarity. Supplementary Material Section 2 provides a description of the thought process behind deciding on the final geometry, as well as stress-strain curves of various intermediate iterations.

The beam element model response of the spherically-jointed structure with Geometry #3 is shown in Fig. 1 (d) as the purple dashed line, and the full 3D stress element simulation response is shown as the purple dotted line. The beam element simulation presents a slightly stiffer response, with a final stress 5.6% higher

than the full 3D stress simulation. This difference is likely because beam elements present a simplified model of deformation, not taking into account sources of deformation that the 3D stress model is able to capture. The beam element simulation has several advantages, however, over the 3D stress model. The runtime with 8 CPUs for the beam element model is about 6 min, where as for the full 3D stress model it is around 20 times longer. It should be noted that this runtime difference significantly compounds with dynamic simulations (Section 2) and with forthcoming lattice simulations. Easy member diameter modification also makes geometry iterations much more straightforward with the beam element model.

A representative experimental compressive response of a structure with the Geometry #3 is shown in Fig. 1 (d) as the purple solid line. Several samples were tested, and as can be expected, slight variations in the response result from differences in manufacturing. A comparison between fabricated samples is shown later in Section 3. In the experiments, the structures can be compressed to 0.48 strain, when the struts begin to touch (densification). Both experimental and numerical results agree favorably with the pin-jointed response. With a structure height of 48.3 mm, the spherically-jointed structure has a mass of 3.75 g, which is less than the pin-jointed structure's mass of 5.75 g. The normalized strain energy by mass of the spherically-jointed structure is therefore about 1.5 times greater than the counterpart pin-jointed structure.

In both the pin-jointed and spherically-jointed structures, the struts are initially bent upon loading. If a column is eccentrically loaded, or if there is an initial bend in the column, the transverse deflection will be nonzero. Because of this, the increase in the load is gradual and asymptotically approaches the critical load at a rate dependent on the degree of eccentricity/initial bending [45]. In the spherically-jointed structure, since the joints are fixed and the "faces" rotate, the struts bend immediately upon loading. The resulting response asymptotically approaches the critical load of the structure. A similar response occurs with a prestressed pin-jointed structure with struts dimensioned for elastic buckling. At a certain prestress, the struts buckle, and as prestress increases, the transverse deflection of the struts increases. Because of this, the response of the structure asymptotically approaches the structure's critical load instead having a sharp buckling point.

Although the pin-jointed structure and the 3D-printable, spherically-jointed structure have similar constitutive responses, they are governed by different properties: The pin-jointed structure is stretch-dominated and prestressed, whereas the spherically-jointed structure is bending-dominated and not prestressed. Thus, the spherically-jointed structure does not have traditional tensegrity traits, such as prestress tunability. However, the pin-jointed and spherically-jointed structures share some useful similarities: (i) The faces rotate during compression, producing low local strains. (ii) The slender struts undergo elastic buckling. These traits allow the structure to withstand high deformations while remaining elastic, like a tensegrity. (iii) Strain energy is distributed evenly throughout the structural members. (iv) The nonlinear buckling response is load-limiting. (v) Finally, both types of structures have very low relative density, allowing formation of extremely lightweight lattices. Relative density is given by the density of the structure divided by the density of the constituent material. The relative densities of the pin-jointed structure (Geometry #2) and spherically-jointed structure (Geometry #3) are 4.9% and 2.5%, respectively.

3. Dynamic response

3.1. Drop test setup

To examine the dynamic response of the 3D-printable, spherically-jointed structure, we designed and built a drop weight testing system (Fig. 2 (a)). The setup consists of a low-friction, vertical rod, guiding a free-falling striker mass, impacting the samples. The mass is custom-made from steel, with the outer diameter chosen to be large enough to impact all top face nodes of the structure, in order to minimize transverse moment of inertia. We fabricated two different strikers, with 100 g and 200 g mass, respectively. The impact velocity is controlled varying the height of the striker above the sample. An accelerometer is placed on top of the mass to record when the mass first touches the structure as well as the deceleration of the mass during impact. It is a triaxial ceramic shear ICP© accelerometer with a sensitivity of 0.47 mV/(m/s^2). The voltage is recorded with an oscilloscope. Since the accelerometer has a mass of 1.0 g, a counterweight is placed opposite on the mass surface. To allow the natural rotation of the sample, the guiding metal rod runs through the center the structure, as shown in Fig. 2 (a).

The structure sits on top of a glass sheet, which serves as a stiff surface extension for the force sensor under it. The metal rod is suspended above the glass plate. The force sensor measures the reaction force on the bottom face. It is an Impact ICP© quartz force sensor with a sensitivity of 11241 mV/kN. To reduce friction between the structure and the glass sheet, a thin liquid layer of acetone is dispensed on the glass sheet shortly before the test.

A PHANTOM© high-speed camera with a framerate of 1000 fps is used to capture the displacement of the falling mass, and thus the top face nodes of the structure. Black markers on a white background are tracked during the fall using the Phantom Camera Control (PCC) software. Calibration is done using a ruler placed in the same focal plane as the markers. Finally, to ensure synchronized time measurement between the camera and oscilloscope data, a switch is triggered when the mass begins to fall, zeroing the time for the oscilloscope and camera.

A dynamic version of the ABAQUS/STANDARD beam simulation was formulated to compare with drop test experiments. The geometry remains the same, and the top and bottom reference points and coupling constraints are the same. The top reference point now has a point mass equal to the impacting mass, and it has an initial velocity equal to the impacting velocity. A dynamic implicit step is used, with nonlinear geometry and moderate dissipation (used for impact problems). Various impact velocities with both a 100 g and 200 g mass were simulated to narrow down the range of velocities for the experiments. The 200 g mass was used for the experiments because it gave more consistent impact velocities for a given height. It also allowed the drop height to be lower to achieve sufficient compression of the sample.

3.2. Results

Samples were fabricated with a height of 48.3 mm. Four samples were impacted with a 200 g mass multiple times at various increasing impact velocities. The impact velocity corresponds to an impact energy (E_i), which is a fraction of the maximum strain energy of the structure (E_m) before densification (320 mJ). The force-time curves at varying impact energies are shown in Fig. 2 (b). The dotted lines show the ABAQUS simulation results, and the solid lines show experimental results.

For both the simulation and experimental results, there is a short lag time before the force increases from zero. This is the transmission time for the wave to travel through the structure, and thus it determines the wave speed for the structure. For the simulations, the wave speed is consistently around 95 m/s, whereas for the experiments the wave speed ranges from about 65 m/s to 135 m/s.

There are oscillations in the force response, both during loading and unloading but more distinct during loading. These oscillations are due to the stress wave travelling back and forth within the structure, vibration of the struts, and rotation of the structure's faces

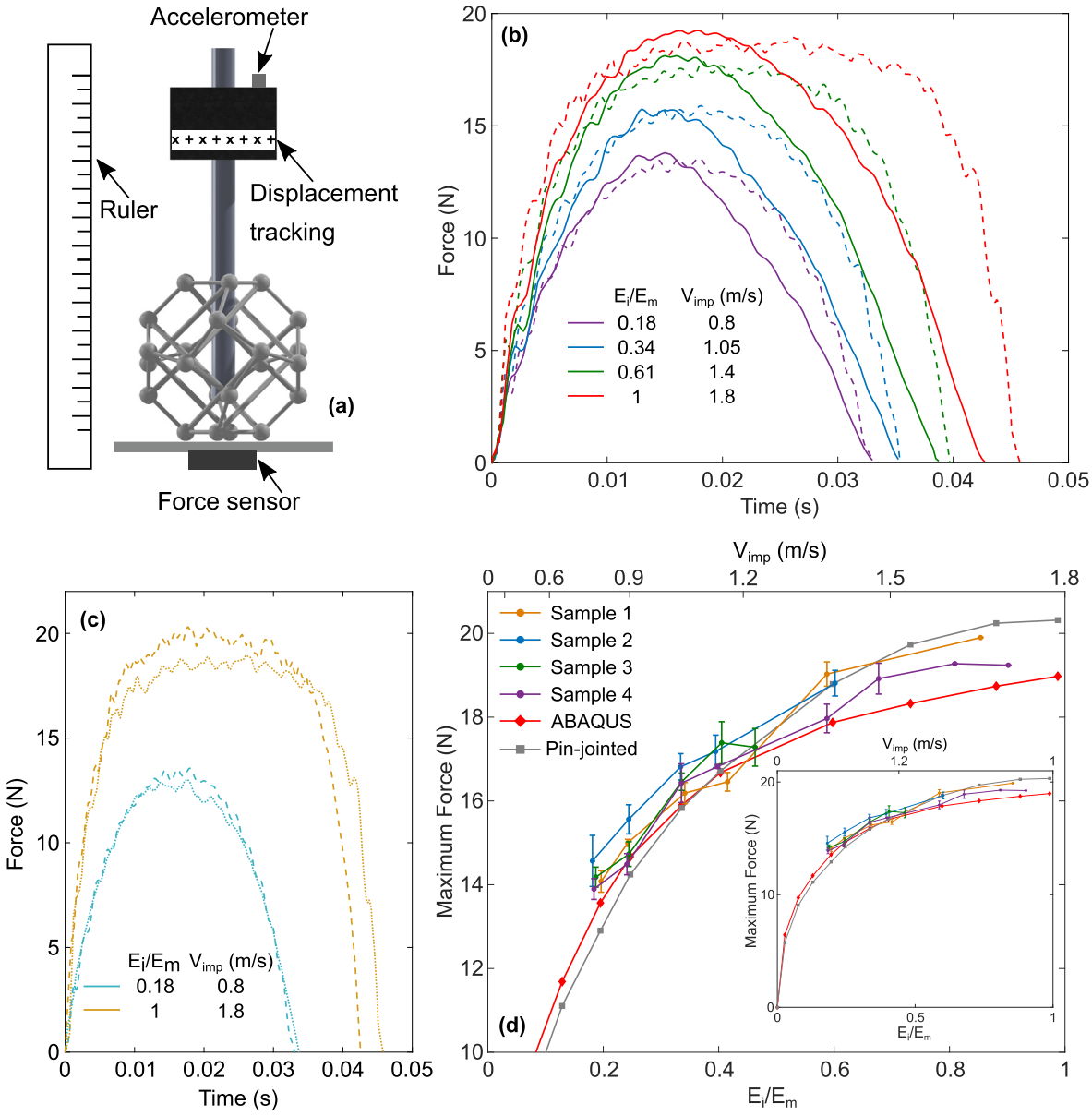

Fig. 2. (a) Drop weight testing system setup. (b) The force-time response of the structure at varying impact energies, as a ratio of the impact energy to the maximum strain energy of the structure before densification. Impacting velocities are also shown, corresponding to the impact energy ratios. The solid lines are experimental curves, and the dashed lines are results of the ABAQUS beam element simulation. The force plateaus to the structure's buckling force as the impact energy increases. (c) Comparison of the pin-jointed structure simulation (solid lines) and the spherically-jointed ABAQUS beam element simulation (dashed lines) for two impact energies. (d) The maximum force exhibited by the structure as a function of the impact energy ratio and impacting velocity. The experimental results of 4 samples are shown with error bars at each impact energy. In the inset plot, the force and impact energy ratio are shown to the origin in order to observe the significant plateau of the maximum force.

during compression. Videos of the experiments show that the structure's top and bottom faces do not smoothly rotate with time, but rotates in distinct stages, contributing to oscillations in the reaction force. This is seen in the Supplementary Material video, which shows the 100 g striker impacting a sample with an impact energy to maximum energy ratio (E_i/E_m) of 1.

At the lower impact energies, the structure does not compress enough to enter the buckling region, so the response does not plateau from buckling. At higher impact energies, most noticeably at an impact energy ratio of 1, there is a significant plateau in the force response due to buckling in the structure. The structure's dynamic response exhibits load-limiting; the load does not exceed the buckling load of the structure.

There are differences between the simulations and experiments. The curves match well during the loading phase, but during unloading the experimental curves drop quickly while the simulation curves mirror their loading phase. In the experiments, energy is dissipated due to internal friction (hysteresis). Due to this, the response is less oscillatory, and the unloading curve "loses energy" (Fig. 2 (b)). The beam element simulation in ABAQUS does not consider hysteresis or plasticity in the material, so the loading and unloading sections do not differ significantly. Thus, the plateau is more readily observed in the simulation. We do not apply hysteresis in the simulation because hysteresis is not implementable with beam elements within ABAQUS. Addition of the hysteresis term would be possible with the full 3D stress simulation. However, due to runtime we switched to the beam element simulation after quasi-static analysis. Also, beam elements will be required for forthcoming simulations of lattices, where the model size would become significantly larger and full 3D stress simulations would become impractical. We

recognize that experiments are vital in this and upcoming work in order to obtain realistic behavior that the simulation cannot provide.

It is important to examine how the quasi-statically equivalent pin-jointed structure compares in the dynamic regime. We found the dynamic response of the pin-jointed structure using the approach developed in Ref. [16]. The results for two impact energies are shown in Fig. 2 (c) with dashed lines along with the ABAQUS simulation results in solid lines. We can see that the pin-jointed response agrees favorably with the spherically-jointed structure response. The impact corresponds very well at the low impact energy, when the structure's response is linear. However, at the high impact energy, the pin-jointed response has a slightly higher force and shorter impact time than the ABAQUS simulation. Overall, the structures behave similarly with nonlinearity due to buckling.

Fig. 2 (d) shows results of the 4 tested samples along with the ABAQUS and pin-jointed simulations. Each sample was tested 3 times at each impact energy, and the maximum force was recorded for each test. The maximum force increases with the impact energy ratio, but a distinct plateau is observed, as is seen in the inset plot. This shows that the desired load-limiting characteristic is exhibited starting at impact energies significantly lower than the maximum energy capacity of the structure ($E_i/E_m = 1$). Also, the experimental results for the four samples agree favorably with the simulation results. This behavior is analogous to the behavior of the maximum force with impact energy for the pin-jointed buckling tensegrity structure described in Ref. [16].

Energy dissipation in the experiments is significant. In Fig. 3, the experimental stress-strain curves for varying impact energy ratios are shown. E_d is the dissipated energy as a percentage of the impact energy. It is clear that energy dissipation is substantial even at low impact energies. This dissipation can be due internal friction (hysteresis), plastic deformation, and friction/damping in the test setup. In order to evaluate the effect of the test setup, we performed experiments with two impacting masses to compare the experimental results. We ran a drop test with the 100 g mass at an impact velocity of 2.1 m/s. This has the same impacting momentum as a 200 g mass with impacting velocity of 1.05 m/s. From the results of both tests, the absorbed momentum values during impact (area under the force time curve) are within 1% of each other. The agreement between the two experiments indicate that the test setup does not contribute significantly to energy loss during impact. The force-time curves of these tests are shown in Supplementary Figure 3, and further discussion is given in Supplementary Section 3.

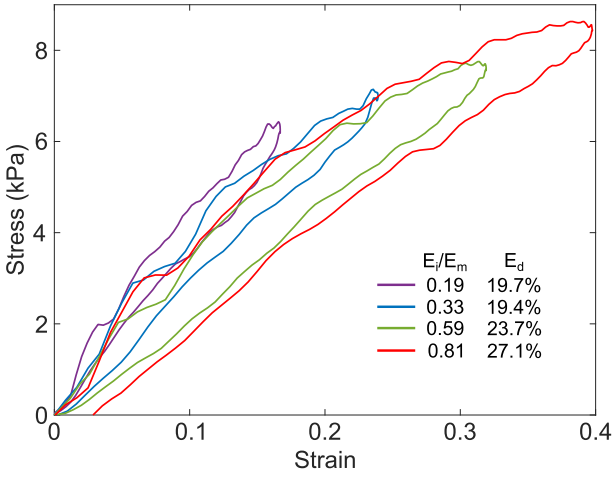

Fig. 3. Experimental dynamic stress-strain curve during impact of the test structure. The energy dissipated as a percentage of the impact energy is listed for each impact energy ratio.

Table 1
The total remaining strain after 24 impacts for each sample, and the average remaining strain after each impact. The structure undergoes little plastic deformation, even after many impacts, showing the resilience and reusability of the structure.

	Total after 24 impacts	**Average after each impact**
Sample 1	1.76%	0.06%
Sample 2	1.66%	0.11%
Sample 3	3.18%	0.15%
Sample 4	2.52%	0.11%
Average	**2.28%**	**0.11%**

For repeated impact applications, one desirable characteristic of tensegrity structures is that they remain elastic even under high deformations. Since an objective for the structure designed in this paper is to be reusable even under high deformation, plastic deformation should be kept to a minimum. As seen in Fig. 3, for the lower three impact energies, strain after unloading is effectively zero. For $E_i/E_m = 0.81$, there is about 3% remaining strain, but this is immediately after the mass separates from the structure. When the remaining strain is measured, one minute later, the remaining strain is effectively zero. This lag in strain is due to the material's viscoelasticity. In Table 1, the remaining strain after 24 impacts and after each impact for a wide variety of impact energies is shown for four samples. After each impact, the remaining strain is less than 0.2%, showing little plastic deformation. Even after 24 impacts, the remaining strain is, on average, 2.28%. This indicates that the structure is reusable and resilient to repeated loading and increasing impact energies. The structure maintains the tensegrity characteristic of an elastic response under high deformation. Because there is little plastic deformation, the dissipated energy during the impact is almost entirely due to hysteresis in the material.

3.3. Energy absorption efficiency

Although the designed spherically-jointed structure has not been optimized for energy absorption performance, a comparison of its energy performance with several types of manufacturable lattice materials is useful and is shown in Fig. 4. Here, the energy absorption efficiency, $W_{\min}$, is defined as [26]:

$$W_{\min} = C_{\min}\,\rho_r \tag{2}$$

where ρ_r is the relative density and $C_{\min}$ is the cushion factor. The cushion factor is given by [26]:

$$C_{\min} = \frac{\sigma}{Q} \tag{3}$$

where σ is the maximum stress of the material's stress strain-curve until failure (e.g., densification, yield, or rupture), and Q is the area under the stress-strain curve up to σ. The minimum value of the cushion factor, $C_{\min}$, represents the maximum impact absorption efficiency of the material, and theoretical limit of $C_{\min}$ for a material is 1. Cushion factor (or its inverse) is often used to asses the energy absorption of porous materials, such as lattices [46,47,50,51]. $W_{\min}$ is also a useful quantity [26] because, like $C_{\min}$, a design with lower $W_{\min}$ indicates better energy absorption. For instance, if two materials have the same $C_{\min}$, and one has a lower $W_{\min}$, the material with lower $W_{\min}$ absorbs the same energy at a given stress but uses less material. This means it offers the lowest mass for equivalent impact absorption.

In Fig. 4, we plot $W_{\min}$ against relative density for several lattices, foams, and solid materials. We define a target region, which is given by a relative density lower than 0.1 and a $W_{\min}$ lower than 0.21. This is chosen for the following reasons. Often, non-metal lattices require

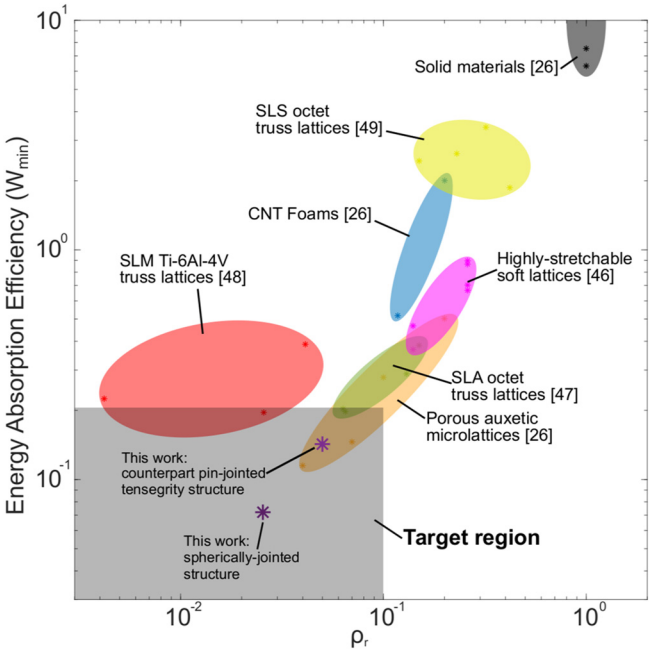

Fig. 4. Energy absorption efficiency (W_{min}) for the spherically-jointed structure and pin-jointed structure presented in this work, as well as for several lattice, foam, and solid materials [26,46-49]. The energy absorption efficiency is given by the cushion factor multiplied by the relative density of the material. The target region is defined by a W_{min} less than 0.21 and relative density less than 0.1 (reasons explained in the text). Solid materials all have a relative density of 1 and their W_{min} extend well beyond the range of this plot, as indicated by the truncated gray oval. The structures presented in this work lie within the target region, with the spherically-jointed structure exhibiting the best energy absorption efficiency of all presented materials, along with a very low relative density.

higher relative densities due to manufacturing constraints and thus commonly have relative densities above 10%. Also, the best available lattice foams have C_{min} values as low as 2.1 [26]. Multiplying C_{min} of 2.1 by a relative density of 0.1 gives a target region limit of $W_{min} = 0.21$. The results of this work lie within this target region, exhibiting remarkable energy efficiency and very low relative densities for polymer structures. Interestingly, the spherically-jointed structure exhibits the lowest W_{min} of all shown structures and the lowest polymer relative density, even compared to its counterpart pin-jointed tensegrity structure. Also, several of the other lattices presented do not elastically deform under impact, but plastically deform, making them non-reusable. The structures designed in this work elastically deform and are reusable under multiple impacts. This shows that, even without optimization of energy absorption, our design shows novel characteristics, making it promising for use in ultra-lightweight, energy absorbing metamaterials.

4. Conclusions

In this paper, we presented a method to overcome manufacturing limitations of tensegrity structures by designing a 3D-printable structure with analogous strain energy capacity and compressive response as a pin-jointed tensegrity structure. The structure design uses spherical joints to separate structural members in a way that maintains certain tensegrity characteristics, allowing the compressive and dynamic responses to behave similarly to a counterpart prestressed buckling tensegrity. The structure is fabricated with a single material, allowing it to be printed with a variety of currently available 3D-printing methods. It has several of the same appealing characteristics of buckling tensegrity structures, including stability post-buckling, resilience to severe deformation, high elastic strain energy absorption, and load-limitation. A drop weight testing system was developed to analyze the dynamic response of the structure. We found that the structure's dynamic response also mimics that of a buckling tensegrity. Simple modification of the member diameters allows straightforward tunability of the structure's mechanical response and strain energy capacity. It should be noted that although the 3D-printable, spherically-jointed structure was designed to be analogous to a certain pin-jointed tensegrity structure, the principles outlined here can be used to design other structures with equivalence to a wide range of tensegrity structures. The unique characteristics of tensegrity structures with buckling struts have been predicted purely theoretically [16] until this point. This paper corroborates the response of buckling tensegrity structures experimentally for the first time.

We conjecture that the tensegrity-inspired structure presented here has potential for use as a unit cell in multidimensional lattices. Periodic media formed by tessellating buckling tensegrity structures show tunable, nonlinear, and dispersive wave propagation characteristics [33-35]. These lattices show great potential for applications such as stress wave management, impact mitigation, and vibration control. Since the structure presented in this paper exhibits comparable quasi-static and dynamic responses to buckling tensegrity structures under impact, lattices formed with this structure might possess similar wave propagation characteristics. Our future work will include manufacturing and testing multidimensional lattices with various fabrication methods and materials.

Without the need for pin-joints or prestress, the structure presented in this paper uses geometry to produce tensegrity-like characteristics. The designed structure provides a way to exploit many useful characteristics of a tensegrity structure without needing cumbersome manufacturing. The structure also exhibits desirable energy absorption characteristics, with excellent energy absorption efficiency and ultra-low relative density. This paper lays the foundation for novel research that will expand the fundamental understanding of energy absorption in buckling tensegrity-inspired metamaterials and provide basic design tools for applications.

CRediT authorship contribution statement

Kirsti Pajunen: Conceptualization, Methodology, Software, Validation, Formal analysis, Investigation, Data curation, Writing - original draft, Writing - review & editing, Visualization, Funding acquisition. **Paul Johanns:** Software, Validation, Formal analysis, Investigation, Data curation. **Raj Kumar Pal:** Methodology, Software, Validation, Formal analysis. **Julian J. Rimoli:** Conceptualization, Methodology, Software, Validation, Supervision. **Chiara Daraio:** Conceptualization, Methodology, Validation, Resources, Visualization, Supervision, Project administration, Funding acquisition.

Acknowledgments

This research was conducted with Government support under and awarded by DoD, Air Force Office of Scientific Research, National Defense Science and Engineering Graduate (NDSEG) Fellowship, 32 CFR 168a.

Appendix A. Supplementary data

Supplementary data to this article can be found online at https://doi.org/10.1016/j.matdes.2019.107966.

Data Availability

The raw/processed data required to reproduce these findings cannot be shared at this time due to technical or time limitations.

References

[1] S. Pellegrino, Deployable Structures, Springer. 2001, 179–198.
[2] J. Zhang, M. Ohsaki, Tensegrity Structures, Springer. 2015, v–vii.
[3] R.E. Skelton, R. Adhikari, J.-P. Pinaud, W. Chan, J.W. Helton, An introduction to the mechanics of tensegrity structures, Proceedings of the 40th IEEE Conference on Decision and Control, 5, IEEE. 2001, pp. 4254–4259.
[4] M. Masic, R.E. Skelton, P.E. Gill, Optimization of tensegrity structures, Int. J. Solids Struct. 43 (2006) 4687–4703.
[5] R. Skelton, F. Fraternali, G. Carpentieri, A. Micheletti, Minimum mass design of tensegrity bridges with parametric architecture and multiscale complexity, Mech. Res. Commun. 58 (2014) 124–132.
[6] K. Nagase, R. Skelton, Minimal mass tensegrity structures, J. Int. Ass. Shell Spatial Struct. 55 (2014) 37–48.
[7] I. Oppenheim, W. Williams, Mechanics of tensegrity prisms, Proceedings of the 14th International Symposium on Automation & Robotics in Construction, 1997.
[8] A. Tibert, S. Pellegrino, Review of form-finding methods for tensegrity structures, Int. J. Space Struct. 18 (2003) 209–223.
[9] A. Tibert, S. Pellegrino, Deployable tensegrity reflectors for small satellites, J. Spacecr. Rocket. 39 (2002) 701–709.
[10] F. Fraternali, G. Carpentieri, A. Amendola, On the mechanical modeling of the extreme softening/stiffening response of axially loaded tensegrity prisms, J. Mech. Phys. Solids 74 (2015) 136–157.
[11] A. Amendola, G. Carpentieri, M. De Oliveira, R. Skelton, F. Fraternali, Experimental investigation of the softening-stiffening response of tensegrity prisms under compressive loading, Compos. Struct. 117 (2014) 234–243.
[12] I. Mascolo, A. Amendola, G. Zuccaro, L. Feo, F. Fraternali, On the geometrically nonlinear elastic response of class $\theta = 1$ tensegrity prisms, Front. Mater. 5 (2018) 16.
[13] H. Furuya, Concept of deployable tensegrity structures in space application, Int. J. Space Struct. 7 (1992) 143–151.
[14] C. Sultan, Modeling, Design, and Control of Tensegrity Structures with Applications, Ph.D. thesis. 1999.
[15] S.H. Juan, J.M.M. Tur, Tensegrity frameworks: static analysis review, Mech. Mach. Theory 43 (2008) 859–881.
[16] J.J. Rimoli, A reduced-order model for the dynamic and post-buckling behavior of tensegrity structures, Mech. Mater. 116 (2018) 146–157.
[17] A. Zhang, B. Cera, A. Agogino, Characterization of six-bar spherical tensegrity lattice topologies, Proceedings of the IASS Symposium 2018: Creativity in Structural Design, 2018.
[18] J.M.M. Tur, S.H. Juan, Tensegrity frameworks: dynamic analysis review and open problems, Mech. Mach. Theory 44 (2009) 1–18.
[19] J. Michielsen, R. Fey, H. Nijmeijer, Steady-state dynamics of a 3D tensegrity structure: simulations and experiments, Int. J. Solids Struct. 49 (2012) 973–988.
[20] C. Sultan, Designing structures for dynamical properties via natural frequencies separation: application to tensegrity structures design, Mech. Syst. Signal Process. 23 (2009) 1112–1122.
[21] S. Faroughi, H.H. Khodaparast, M.I. Friswell, Non-linear dynamic analysis of tensegrity structures using a co-rotational method, Int. J. Non Linear Mech. 69 (2015) 55–65.
[22] I.J. Oppenheim, W.O. Williams, Vibration of an elastic tensegrity structure, Eur. J. Mech. A. Solids 20 (2001) 1023–1031.
[23] I.J. Oppenheim, W.O. Williams, Vibrations and design of tensegrity structures, Rev. Fr. Genie Civil 7 (2003) 377–389.
[24] K.T. Tan, H. Huang, C. Sun, Blast-wave impact mitigation using negative effective mass density concept of elastic metamaterials, Int. J. Impact Eng. 64 (2014) 20–29.
[25] S. Cui, B. Gong, Q. Ding, Y. Sun, F. Ren, X. Liu, Q. Yan, H. Yang, X. Wang, B. Song, Mechanical metamaterials foams with tunable negative Poisson's ratio for enhanced energy absorption and damage resistance, Materials 11 (2018) 1869.
[26] C.Q. Lai, C. Daraio, Highly porous microlattices as ultrathin and efficient impact absorbers, Int. J. Impact Eng. 120 (2018) 138–149.
[27] F. Fraternali, L. Senatore, C. Daraio, Solitary waves on tensegrity lattices, J. Mech. Phys. Solids 60 (2012) 1137–1144.
[28] F. Fraternali, G. Carpentieri, A. Amendola, R.E. Skelton, V.F. Nesterenko, Multiscale tunability of solitary wave dynamics in tensegrity metamaterials, Appl. Phys. Lett. 105 (2014) 201903.
[29] C. Davini, A. Micheletti, P. Podio-Guidugli, On the impulsive dynamics of T3 tensegrity chains, Meccanica 51 (2016) 2763–2776.
[30] F. Fabbrocino, G. Carpentieri, Three-dimensional modeling of the wave dynamics of tensegrity lattices, Compos. Struct. 173 (2017) 9–16.
[31] A. Amendola, A. Krushynska, C. Daraio, N.M. Pugno, F. Fraternali, Tuning frequency band gaps of tensegrity mass-spring chains with local and global prestress, Int. J. Solids Struct. 155 (2018) 47–56.
[32] A. Krushynska, A. Amendola, F. Bosia, C. Daraio, N. Pugno, F. Fraternali, Tunable extremely wide low-frequency band gaps in accordion-like metamaterials, 2018 12th International Congress on Artificial Materials for Novel Wave Phenomena (Metamaterials), IEEE. 2018, pp. 237–239.
[33] J.J. Rimoli, R.K. Pal, Mechanical response of 3-dimensional tensegrity lattices, Compos. Part B 115 (2017) 30–42.
[34] R.K. Pal, M. Ruzzene, J.J. Rimoli, Tunable wave propagation by varying prestrain in tensegrity-based periodic media, Extreme Mech. Lett. (2018).
[35] H. Salahshoor, R.K. Pal, J.J. Rimoli, Material symmetry phase transitions in three-dimensional tensegrity metamaterials, J. Mech. Phys. Solids 119 (2018) 382–399.
[36] V. SunSpiral, G. Gorospe, J. Bruce, A. Iscen, G. Korbel, S. Milam, A. Agogino, D. Atkinson, Tensegrity based probes for planetary exploration: entry, descent and landing (EDL) and surface mobility analysis, Int. J. Planetary Probes 7 (2013).
[37] A. Campesato, Unprecedented structural skins. Experiments towards an intelligent tensegrity skin, Procedia Eng. 155 (2016) 183–194.
[38] A. Amendola, E. Hernandez-Nava, R. Goodall, I. Todd, R. Skelton, F. Fraternali, On the additive manufacturing, post-tensioning and testing of bi-material tensegrity structures, Compos. Struct. 131 (2015) 66–71.
[39] K. Liu, J. Wu, G.H. Paulino, H.J. Qi, Programmable deployment of tensegrity structures by stimulus-responsive polymers, Sci. Rep. 7 (2017) 3511.
[40] H. Xu, D. Pasini, Structurally efficient three-dimensional metamaterials with controllable thermal expansion, Sci. Rep. 6 (2016) 34924.
[41] A.A. Bauhofer, S. Krödel, J. Rys, O.R. Bilal, A. Constantinescu, C. Daraio, Harnessing photochemical shrinkage in direct laser writing for shape morphing of polymer sheets, Adv. Mater. 29 (2017) 1703024.
[42] Y. Li, X.-Q. Feng, Y.-P. Cao, H. Gao, Constructing tensegrity structures from one-bar elementary cells, Proc. Roy. Soc. A Math. Phys. Eng. Sci. 466 (2009) 45–61.
[43] R.E. Skelton, M.C. de Oliveira, Tensegrity Systems, Springer. 2009, 3.
[44] R. Budynas, K. Nisbett, Shigley's Mechanical Engineering Design, McGraw-Hill Education. 2010.
[45] J.M. Gere, B.J. Goodno, Mechanics of Materials, Cengage Learning, USA, 2012.
[46] Y. Jiang, Q. Wang, Highly-stretchable 3D-architected mechanical metamaterials, Sci. Rep. 6 (2016) 34147.
[47] M. Mohsenizadeh, F. Gasbarri, M. Munther, A. Beheshti, K. Davami, Additively-manufactured lightweight metamaterials for energy absorption, Mater. Des. 139 (2018) 521–530.
[48] I. Ullah, M. Brandt, S. Feih, Failure and energy absorption characteristics of advanced 3D truss core structures, Mater. Des. 92 (2016) 937–948.
[49] Y. Sha, L. Jiani, C. Haoyu, R.O. Ritchie, X. Jun, Design and strengthening mechanisms in hierarchical architected materials processed using additive manufacturing, Int. J. Mech. Sci. 149 (2018) 150–163.
[50] L.J. Gibson, M.F. Ashby, Cellular Solids: Structure and Properties, Cambridge University Press. 1999.
[51] N. Nayak, D. Tripathy, Deformation and energy absorption characteristics of microcellular ethylene-octene copolymer vulcanizates, Polym. Eng. Sci. 42 (2002) 1274–1285.